

Article

Aerodynamics and Sealing Performance of the Downstream Hub Rim Seal in a High-Pressure Turbine Stage

Filippo Merli ¹, Nicolas Krajnc ¹, Asim Hafizovic ¹, Marios Patinios ² and Emil Göttlich ^{1,*}

¹ Institute of Thermal Turbomachinery and Machine Dynamics, Graz University of Technology, Inffeldgasse 25A, 8010 Graz, Austria

² GE Aviation, Freisinger Landstrasse 50, 85748 Garching bei München, Germany

* Correspondence: emil.goettlich@tugraz.at

Abstract: The purpose of the paper is to characterize the aerodynamic behavior of a rotor-downstream hub cavity rim seal in a high-pressure turbine (HPT) stage. The experimental data are acquired in the Transonic Test Turbine Facility at the Graz University of Technology: the test setup includes two engine-representative turbine stages (the last HPT stage and first LPT stage), with the intermediate turbine duct in between. All stator-rotor cavities are supplied with purge flows by a secondary air system, which simulates the bleeding air from the compressor stages of the real engine. The HPT downstream hub cavity is provided with wall taps and pitot tubes at different radial and circumferential locations, which allows the performance of steady pressure and seed gas concentration measurements for different purge mass flows and HPT vanes clocking positions. Moreover, miniaturized pressure transducers are adopted to evaluate the unsteady pressure distribution, and an oil flow visualization is performed to retrieve additional information on the wheel space structures. The annulus pressure asymmetry depends on the HPT vane clocking, but this is shown to have negligible impact on the minimum purge mass flow required to seal the cavity. However, the hub pressure profile drives the distribution of the cavity egress in the turbine channel. The unsteady pressure field is dominated by blade-synchronous oscillations. No non-synchronous components with comparable intensity are detected.

Keywords: cavity; wheel space; purge; rim seal; turbine; aerodynamics; concentration effectiveness; oil flow visualization



Citation: Merli, F.; Krajnc, N.; Hafizovic, A.; Patinios, M.; Göttlich, E. Aerodynamics and Sealing Performance of the Downstream Hub Rim Seal in a High-Pressure Turbine Stage. *Int. J. Turbomach. Propuls. Power* **2023**, *8*, 20. <https://doi.org/10.3390/ijtp8030020>

Academic Editors: Tony Arts and Rodolfo Bontempo

Received: 9 May 2023
Revised: 11 June 2023
Accepted: 23 June 2023
Published: 10 July 2023



Copyright: © 2023 by the authors. Licensee MDPI, Basel, Switzerland. This article is an open access article distributed under the terms and conditions of the Creative Commons Attribution (CC BY-NC-ND) license (<https://creativecommons.org/licenses/by-nc-nd/4.0/>).

1. Introduction

In the continuous effort to achieve higher thermal efficiencies, modern turbofan engines underwent a significant increase in turbine inlet temperatures over the last decades. The trend strengthens the importance of cooling flows in both high-pressure (HPT) and low-pressure (LPT) turbines. In state-of-the-art turbofans, an internal secondary air system redirects fluid from the main stream of different compressor stages to the turbine stator-rotor cavities. A fraction of the secondary air, often referred to as sealing or purge flow, is used to prevent hot main gas ingestion through the rim seals, normally placed between the rotor disks and the stator platforms. It helps maintain the internal metal temperatures within a limit that safeguards the integrity and life of the components. The interaction between sealing and main stream flow is known to produce a drop in turbine efficiency. Consequently, it is of interest for engine designers to use the minimum purge mass flow rate to seal the cavities. At the same time, it is crucial to investigate the aerothermal behavior inside the stator-rotor cavities, to understand the ingress and egress mechanism and further reduce the efficiency loss. This study aims to address the mentioned designer needs by:

- evaluating the sealing performance of the rim seal in the rotor-downstream hub cavity (DHC) of a high-pressure turbine stage;
- characterizing the aerodynamics inside the same HPT cavity.

The HPT stage is integrated into an engine-representative two-stage turbine, including an intermediate turbine duct with turning struts, to guarantee realistic conditions, especially in terms of annulus Mach number. Wall taps are distributed inside the DHC and on the corresponding stator hub platform to retrieve pressure and concentration effectiveness data. Furthermore, unsteady pressure sensors and oil flow visualization are utilized to get a deeper insight into the cavity flow field. Several purge flow rates are analyzed, as well as multiple HPT vane and strut clocking settings. To the extent of the authors' knowledge, the combination of the described measurement techniques with the wide range of operating conditions applied within such a relevant test vehicle is a *unicum* in the open turbomachinery literature and is expected to provide original information to the engine manufacturers.

2. Brief Literature Review

According to Owen [1], the ingress of main air into the wheel space can be of three types:

- Externally induced, when it is caused by annulus (external) flow asymmetries, e.g., the ones caused by the presence of a vane row in a turbine stage;
- Rotationally induced, when the rotating fluid in the cavity generates a pressure gradient, such that a radial outflow arises near the rotor (disk pumping) and ingress happens close to the stator wall;
- Combined ingress, when externally and rotationally induced ingress, is of the same order of magnitude.

The externally driven ingress is generally the dominant type in conventional turbines, especially with single-rim seals (double-rim seals may show rotationally induced ingress for the inner one).

Given the detrimental effect of the sealing flow on the turbine efficiency (Regina et al. [2] estimated a 0.8% drop for each injection rate percent), many researchers focused on the prediction of the minimum sealing flow rate necessary to prevent externally induced ingress. Phadke and Owen [3] found that, for non-axisymmetric external flow, the minimum non-dimensional sealing flow, $C_{0,min} = \dot{m}_{0,min} / \mu b$, is independent of the rotational Reynolds number, Re_{Ω} , and increasing with the annulus bulk Reynolds number, Re_W . They also obtained a correlation between $C_{0,min}$, Re_W and the maximum non-dimensional pressure asymmetry $\Delta C_{P,max}$:

$$C_{0,min} = 2\pi K G_c Re_W (0.5 \Delta C_{P,max})^{0.5}, \quad (1)$$

where the parameter $K = 0.6$ produced a good fitting for different seal geometries in a vaneless and bladeless case. Bohn and Wolff [4] adopted the same correlation inside a turbine setup with vanes and blades. They found a higher dependence of K on the tested seal configurations. Hamabe and Ishiba [5] provided one of the first examples of ingress and egress modeling through separate orifices, where the associated discharge coefficients were determined empirically. Many research groups then developed and tuned orifice models to evaluate the seal performance ([1,6] among others).

More recently, Scobie et al. [7] investigated the egress-main flow interaction in the downstream hub cavity of a turbine stage. They measured an asymmetric egress distribution in the annulus at the edge of the seal clearance, driven by the annulus pressure profile. Scobie et al. [8] quantified the re-ingestion of the upstream hub cavity purge into the downstream one, using seed gas concentration measurements. They concluded that the upstream injection partially mixes with the annulus air stream close to the downstream seal, reducing the adverse effects of ingress. In any case, many of the experimental works on the subject are performed in facilities operating at low speed, with annulus Mach number ranging approximately from $M = 0.2$ to 0.4 upstream of the rotor blade [9,10] and $M < 0.2$ downstream [7,11].

In terms of the cavity's unsteady flow field, many experimental and numerical studies [12–15] identified unsteady rim seal rotating structures whose frequency is unrelated to the blade passing or disk frequency. Despite the exact nature of these structures still

being debated, they are often attributed to Kelvin–Helmholtz instabilities [16] or inertial waves [17] at the rim seal region. In his review paper, Chew [18] observed that simple, high-clearance axial seals normally show lower non-synchronous frequencies, while the opposite holds for more complex and tight seals. However, not all the available literature was found to fit the trend.

3. Experimental Setup

3.1. Facility and Test Vehicle

The measurement campaign is carried out in its entirety in the Transonic Test Turbine Facility (TTTF) of the Graz University of Technology (Institute of Thermal Turbomachinery and Machine Dynamics, ITTM). The TTTF is a dual-spool, continuous, open-circuit test bench historically devoted to the aerothermal investigation of intermediate turbine frames [19–21]. The main flow is supplied to the turbine by a 3 MW compression station, while a 560 kW suction blower, placed downstream of the test section, allows to decrease and stabilize the backpressure against ambient condition variations. In the two-stage arrangement, the TTTF's high-pressure shaft speed is controlled by a radial brake compressor, whose outflow is mixed with the compressor station flow in a settling chamber and then fed to the test section. The resulting maximum pressure and mass flow rate at the inlet of the turbine are 4 bar and 22 kg/s, respectively. On the other side, the low-pressure turbine speed is regulated with a 700 kW water brake.

A secondary air system, supplied by a 1.1 kW electric compressor, provides up to 2.5 kg/s of purge air to six different lines, with the independent mass flow and temperature control. Each purge line is connected via independent regulation valves to two pressurized reservoirs containing CO₂ and N₂O, respectively. They are used to seed the cavity flows and perform concentration measurements, as described in the Measurement Techniques section. Further details about the TTTF are available in Hubinka et al. [22] and Steiner et al. [23].

The test section, in which the measurements are taken, is sketched in Figure 1. It consists of a fully purged, two-stage turbine, aerodynamically representative of the last high-pressure turbine (HPT) stage, the intermediate turbine duct, and the first low-pressure turbine (LPT) stage in a state-of-the-art turbofan engine. In particular, the HPT stage vane and blade counts are indicated as V and B_1 , respectively, while B_2 is the LPT stage blade count. The intermediate turbine duct is populated by S strut fairings, which integrate the turning function of the LPT stage vane row. Such a setup is commonly known as turbine vane frame (TVF) or turning mid-turbine frame. The TVF struts are interspersed with splitters (SP), two for each strut passage, to reduce the strut loading without introducing excessive blockage at the duct inlet. The HPT stage features four stator-rotor cavities: the upstream and downstream hub cavities (UHC and DHC in the figure) are radial-clearance rim seals, while the upstream and downstream shroud cavities (USC and DSC) are continuous 360° axial slots. All of them can be fed with independent purge streams, as well as the LPT hub cavities. For the purpose of this study, the attention is focused on the flow field of the DHC, which is highlighted by the red rectangle in Figure 1.

3.2. Cavity Geometry and Instrumentation

The detailed DHC geometry is illustrated in Figure 2a, which also includes the cavity instrumentation radial-axial layout. The table on the right side of the figure contains a list of geometric parameters made non-dimensional using the rotor lip inner radius, b . An inner axial seal, with $G_{c,in} > G_{c,z}$, homogenizes the coolant before entering the outer part of the cavity. Finally, Figure 2b reports the circumferential occurrence of the instrumentation presented below.

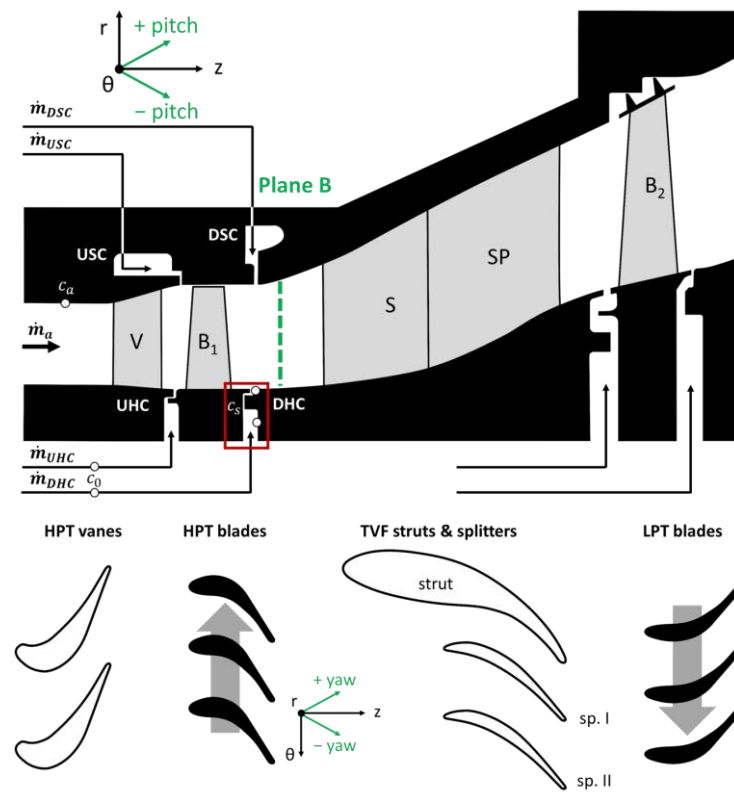


Figure 1. Test section scheme.

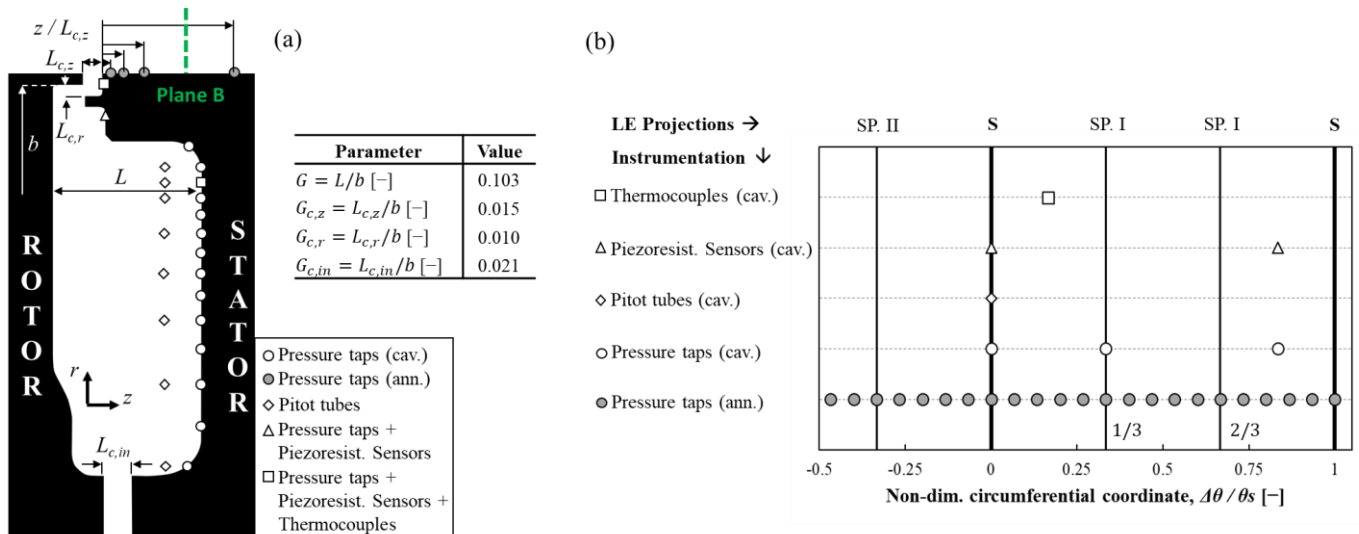


Figure 2. HPT downstream hub cavity instrumentation layout: (a) radial distribution (left), with a list of relevant geometric parameters (top-right); (b) circumferential distribution.

3.2.1. Time-Averaged Pressure Measurements

Static pressure values inside the DHC are obtained using wall taps located on the TVF stator platform. Three radial arrays of taps, circumferentially positioned in correspondence with the strut leading edge (LE), the splitter I LE, and the splitter II-strut mid-passage, are available. In terms of non-dimensional circumferential coordinates, they are at $\Delta\theta_S/\theta_S = (\theta - \theta_{LE,S})/\theta_S = 0, 1/3, 5/6$ respectively, where $\theta_S = 2\pi/S$ is the strut pitch and $\theta_{LE,S}$ is the position of the strut LE. Each tap array is constituted by 16 elements (white circles), distributed between $x = 0.74$ and $x = 1$, where $x = r/b$ is the non-dimensional radial coordinate. At $\Delta\theta_S/\theta_S = 0$, a radial array of pitot tubes is placed in correspon-

dence with some of the wall pressure taps, sampling the flow 10 mm away from the stator wall, as indicated by the white diamonds in Figure 2a. On the TVF hub platform, four circumferential arrays, with 23 wall pressure taps each (grey circles), cover $1.5 \cdot \theta_S$, at the non-dimensional axial coordinates $z/L_{c,z} = 0.28, 0.71, 2.12, 6.36$. The time-averaged pressures are acquired with NetScanner 9116 Pressure Scanners (FS 30 psi, uncertainty $\pm 0.05\%$ FS). For every operating point and measurement location, 30 values are sampled at 5 Hz and then averaged to get the desired pressure readings.

3.2.2. Concentration Measurements

Concentration measurements are performed to calculate the concentration effectiveness ε . After seeding the DHC purge flow, the wall pressure taps (white and grey circles in Figure 2a) can be connected to a gas analyzer to retrieve concentration values. In this experimental campaign, a Siemens Ultramat 6E gas analyzer is employed. Its dual channel configuration allows for the simultaneous concentration measurement of two seed gases (CO_2 and N_2O) from the same air sample. The channels are calibrated using N_2 as zero gas, and the analyzer is kept in an air-conditioned cabinet to remove the effect of ambient temperature variations. The concentration at each measurement point is the average of 5 values, acquired at 1 Hz. The propagated uncertainty on the effectiveness can be assumed: roughly equal to 0.003 for $\varepsilon < 0.1$, linearly varying from 0.003 to 0.013 for $0.1 \leq \varepsilon \leq 1$. More details about the measurement technique are provided by Patinios et al. [24].

3.2.3. Time-Resolved Pressure Measurements

The unsteady pressure field in the DHC is evaluated through two radial sets of Kulite XCQ-062-25D miniaturized piezoresistive transducers (FS 25 psi). A set is placed in front of the strut LE ($\Delta\theta_S/\theta_S = 0$), while the other is at $\Delta\theta_S/\theta_S = 1/3$, in front of splitter I leading edge. Each array includes three sensors, at $x = 0.92, 0.98, 1$, represented by the white triangles in Figure 2a. The unsteady signals are amplified with an Endevco Model 136 and then acquired with a NI PCI-6123 I/O Device, together with the shaft encoders. The sampling frequency and duration are 500 kHz and 2 s. Finally, the extended uncertainty associated with the time-resolved pressure measurements is estimated as $\pm 0.2\%$ FS.

3.2.4. Oil Flow Visualization

To illustrate the surface flow on the cavity walls and on the TVF hub platform, an oil flow visualization is carried out after the aerodynamic and concentration tests. Once the desired operating condition is set, a viscous mixture of motor oil and titanium dioxide (TiO_2) is simultaneously injected into the DHC through 10 of the wall taps displayed in Figure 2a. The mixture has to be liquid enough to be transported by the surface flow across the stator wall, delineating the shear stress trajectories. At the same time, the mixture should be viscous enough not to be immediately blown away by the flow as soon as it enters the test section. After about 20 min, when the oil has dried up and the pigment is fixed, the rig is shut down, disassembled, and documented with pictures.

3.3. Operating Conditions

A broad range of operating conditions is considered to fully characterize the DHC nominal and off-design behavior. More specifically, the annulus flow coefficient and the rotational Reynolds number

$$C_F = \frac{Re_W}{Re_\Omega} = \frac{W}{\Omega b} \quad \text{and} \quad Re_\Omega = \frac{\rho \Omega b^2}{\mu} \quad (2)$$

are kept constant, while 15 different sealing flow rates are investigated, extending from $PFR = 0$ to $PFR = 2$, where

$$PFR = \frac{\dot{m}_0}{\dot{m}_{0,nominal}} \quad (3)$$

and the subscript 0 refers to the purge mass flow rate injected in the considered cavity. The annulus inlet mass flow is measured with two Venturi flow meters (uncertainty $\pm 2\%$), quantifying the main compressor station and HPT brake compressor flows to the turbine intake. The cavity injection rates are determined with McCrometer's V-Cone flow meters ($\pm 0.5\%$), one for each purge supply line. In terms of non-dimensional sealing parameters and turbulent flow parameters,

$$\Phi_0 = \frac{C_0}{2\pi G_c Re_\Omega} = \frac{\dot{m}_0 / (\mu b)}{2\pi G_c Re_\Omega} \text{ and } \lambda_T = C_0 Re_\Omega^{-0.8} \quad (4)$$

the abovementioned *PFR* interval corresponds to $\Phi_0 = 0$ to 0.135 and $\lambda_T = 0$ to 0.249.

Table 1 summarizes the operating conditions for five of the considered operating points (*PFR* = 0, 0.5, 1, 1.5, 2). The nominal (*PFR* = 1) Φ_0 and λ_T values are in line with the $C_{0,min}$ prediction from the simple relation

$$C_{0,min} = 0.61 G_{c,r} Re_\Omega, \quad (5)$$

originally developed by Bayley and Owen [25] for axial clearance rim seals and no annulus flow. According to Daily and Nece [26], the tested gap ratio G and rotational Reynolds number Re_Ω guarantee turbulent flow in the wheel space, with separated boundary layers. The cavity-to-annulus temperature ratio is confined between 0.9 and 1.1, depending on the *PFR*. Moreover, it is noteworthy that, while the DHC parameters are varied, Φ_0 and λ_T are maintained at the nominal point for the other purged HPT and LPT cavities throughout all the considered test cases. The inlet total temperature, the inlet-to-outlet total pressure ratio, and the rotational speeds of the two rotors are also kept constant for all the tests, with an uncertainty of ± 0.3 °C, $\pm 0.5\%$, and $\pm 0.1\%$, respectively. In terms of main stream quantities, the annulus Mach number is approximately $M \approx 0.5$, much higher than the values reported in [7,11].

Table 1. Investigated flow operating conditions.

Case	<i>PFR</i> = 0	<i>PFR</i> = 0.5	<i>PFR</i> = 1	<i>PFR</i> = 1.5	<i>PFR</i> = 2
C_F [–]			0.653		
Re_Ω [–]			3.22×10^6		
Φ_0 [–]	0	0.034	0.068	0.100	0.135
λ_T [–]	0	0.062	0.125	0.185	0.249

In addition to the *PFR* variation, four different HPT vanes clocking positions are investigated. The HPT vanes are, in fact, mounted on a rotatable casing, which allows the operators to modify the strut-vane relative displacement and study its effect on the cavity flow field. The analyzed clocking cases, sketched in Figure 3, are $\Delta\theta_V/\theta_V = (\theta - \theta_{des,V})/\theta_V = 0, 0.2, 0.45, 0.7$, where $\theta_V = 2\pi/V$ is the HPT vane pitch and $\theta_{des,V}$ is the design reference position. At the same time, strut clocking investigations are performed by comparing the results of different radial arrays in the DHC (with fixed *PFR* and HPT vane clocking position).

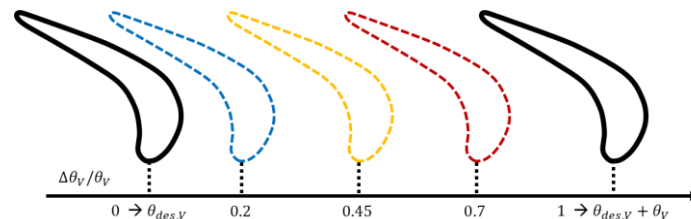


Figure 3. Scheme of the investigated HPT vane clocking positions.

4. Methodology

The static pressure values obtained from the taps listed in the previous section are expressed in terms of the pressure coefficient:

$$C_P = \frac{P - P_{ref}}{0.5\rho\Omega^2 b^2}, \quad (6)$$

where P_{ref} is a reference pressure value arbitrarily chosen by the authors and kept constant throughout all the operating conditions. However, the selected P_{ref} is different between the measurements inside ("cav." in Figure 2b) and outside ("ann.") of the DHC. The tangential speed inside the inviscid core flow in the cavity is calculated with

$$V_\theta = \sqrt{\frac{2(P_T - P)}{\rho}}, \quad (7)$$

using the readings from the pitot tubes and the corresponding wall pressure taps. The swirl ratio is then calculated as follows:

$$\beta = \frac{V_\theta}{\Omega r} \quad (8)$$

According to the ISRE (Isentropic Simple Radial Equilibrium) theory [27], the radial momentum equation for the rotating core returns

$$\frac{1}{\rho} \frac{dP}{dr} = \frac{V_\theta^2}{r}, \quad (9)$$

which can be integrated across the probed radial extent ($x = 0.74 - 1$), to obtain another expression for the swirl ratio, in this case, based only on the wall static pressure distribution:

$$C_{P,x=1} - C_{P,x=0.74} = 2 \int_{x=0.74}^{x=1} x\beta^2 dx \quad (10)$$

The circumferential pressure variations, measured with the wall tap sets on the TVF platform, are associated with a combination of two sources:

- the downstream propagation of the HPT vanes pressure distribution;
- the potential upstream effect of the TVF strut.

Merli et al. [28] show that the upstream effect of the splitters is negligible in Plane B, close to the locations probed in this paper. To discern the impact of the HPT vanes from one of the struts onto the TVF hub platform pressure distribution, an analytical model is introduced. The model (analogous to the one shown in [28]) interprets the circumferential pressure profile as the superposition of two sinusoidal contributions, HPT vanes, and TVF struts, with different amplitude k , phase shift φ , and periodicity:

$$C_P(\theta) = \bar{C}_P + k_V \cos[V(\theta + \varphi_V)] + k_S \cos[S(\theta + \varphi_S)] \quad (11)$$

The model is fit to the experimental data in MATLAB [29], using a nonlinear least-squares procedure, to estimate the values of k_V , k_S , φ_V and φ_S . It should be mentioned that the geometric vane-strut clocking is known, therefore φ_V and φ_S are constrained to $\pm\theta_V/2$ and $\pm\theta_S/2$ around the respective geometric value: this solves the uncertainty related to the periodic nature of the sinusoidal function while keeping a certain flexibility on φ_V and φ_S , to account for non-axial propagation of vanes and struts pressure fields. It is also worth mentioning that, in the charts showing circumferential variations of quantities, the positive direction of θ is against the rotor revolution, as specified in Figure 1.

The concentration effectiveness profiles, reported in the Results and Discussion section, are obtained from

$$\varepsilon = \frac{c_s - c_a}{c_0 - c_a}, \quad (12)$$

where c_s is the seed gas concentration retrieved from the sampled air in the test section, c_0 is the seed gas concentration in the purge supply line (upstream of the cavity) and c_a is the seed gas concentration in the annulus flow (not artificially seeded). The measurement locations of c_0 and c_a are specified in Figure 1. $\varepsilon = 1$ means that $c_s = c_0$, i.e., the sample contains undiluted sealing flow, while $\varepsilon = 0$ ($c_s = c_a$) signifies absence of the seeded cavity supply. Values in the range $0 < \varepsilon < 1$ indicated the presence of purge flow in the sampled air, diluted with the mainstream flow.

Finally, the unsteady pressure readings of the piezoresistive sensors are reported as non-dimensional pressure fluctuations:

$$C'_p(t) = \frac{P(t) - \bar{P}}{P_{ref}} \tag{13}$$

and they are illustrated in the frequency domain after the application of a discrete Fourier transform (DFT).

5. Results and Discussion

The Results and Discussion section is divided into three subsections: the first one describes the time-averaged field inside the DHC; the second one the time-averaged measurements on the stator platform downstream of the DHC; the third one the unsteady pressure field characterizing the DHC.

5.1. Time-Averaged Flow Inside the DHC

5.1.1. Effect of the Sealing Flow Rate

Figure 4a describes the impact of the PFR onto the pressure coefficient radial profile at $\Delta\theta_S/\theta_S = 0$. The average pressure level in the cavity increases with higher purge mass flow rates, while the slope of the profiles decreases with higher coolant injection. Both effects reduce the ingress of annulus flow inside the wheel space, improving the sealing performance. Focusing on the taps at $x = 0.98$ and $x = 1$, respectively inside and outside of the seal lip, a large pressure difference $C_{p,x=1} - C_{p,x=0.98} > 0$ is visible for $PFR = 0$, signifying an important ingestion of main stream flow. The pressure gradient progressively decreases moving towards $PFR = 2$, where the difference becomes negative, suggesting that ingress is locally suppressed. Between the two extremes, it should be possible to find the minimum purge flow rate that maximizes the sealing effectiveness.

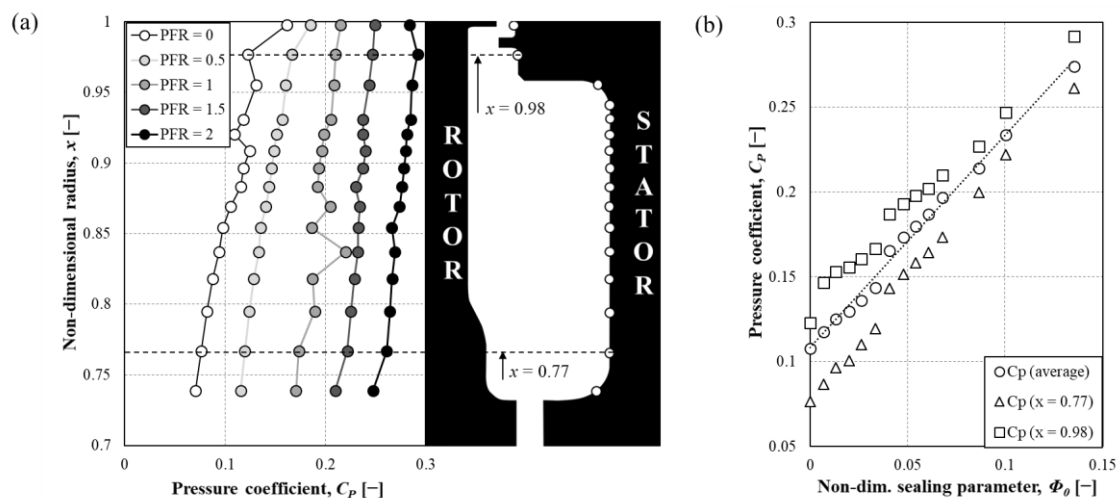


Figure 4. Pressure coefficient inside the DHC: (a) radial profiles with varying PFR. Data are acquired at $\Delta\theta_S/\theta_S = 0$ and $\Delta\theta_V/\theta_V = 0$; (b) pressure coefficient as a function of the sealing flow rate parameter (radial average and local values at $x = 0.77, 0.92$).

Figure 4b shows the variation of the radially averaged pressure coefficient with the non-dimensional sealing parameter (white circles). In agreement with Beard et al. [15], the data are well represented by a straight line (the linear regression’s coefficient of determination is $R^2 = 0.9931$). Such a line is a good estimator of the trend across the full radial extent, especially at high injection rates. In fact, the markers of $C_{P,x=0.77}$ (white triangles) and $C_{P,x=0.98}$ (white squares) are enclosed in relatively narrow intervals around the average values.

The radial development of the DHC swirl ratio β is depicted in Figure 5a. The maximum values are reached for $PFR = 0$ (white circles), with an overall decrease of the swirl ratio across x at higher PFR s. This trend has been reported, among others, by Sangan et al. [30] and Patinios et al. [31] for several seal configurations. For the case without injection, the average β between $x = 0.79$ and $x = 0.89$ is 0.41, approaching the theoretical (0.44) and experimental (0.43) values found by Daily and Nece [26] in an enclosed rotating disk with similar G and Re_Ω . At $x = 0.74$ and $x = 0.93$, the profile diverges from the theoretical threshold because of the proximity to the inner and outer seals, respectively. The swirl ratio data in Figure 5a are pitot-based, meaning that they are obtained from both static and total pressure measurements, according to Equations (7) and (8).

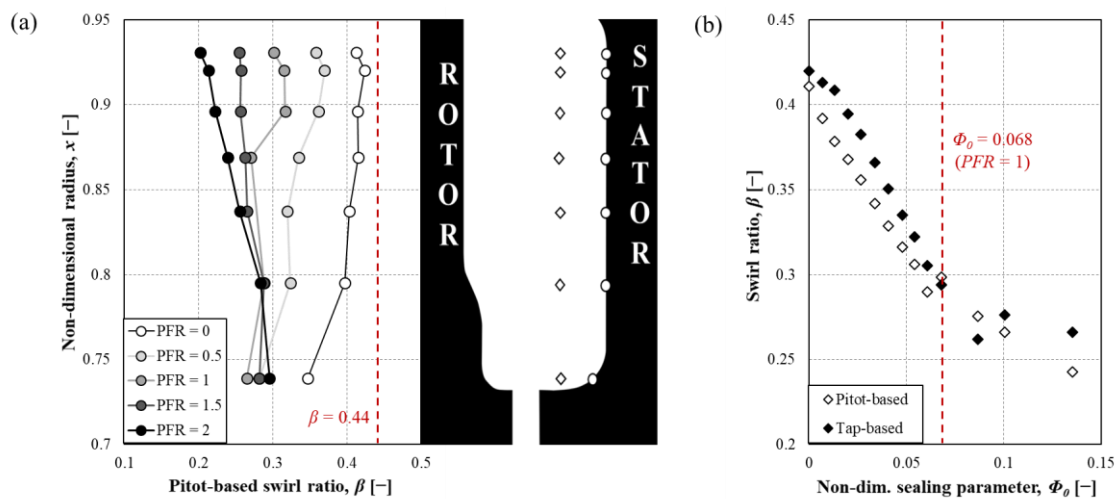


Figure 5. Swirl ratio inside the DHC: (a) radial profiles with varying PFR. Data are acquired at $\Delta\theta_S/\theta_S = 0$ and $\Delta\theta_V/\theta_V = 0$; (b) radially averaged swirl ratio as a function of the sealing flow rate parameter (pitot-based and tap-based calculation).

Figure 5b displays the comparison between the pitot-based swirl ratio (white diamonds, radially averaged) and the swirl ratio estimated as per Equation (9), i.e., purely based on the wall taps readings (black diamonds). The pitot-based and tap-based results are in good agreement, showing the same response to the PFR variation. When the sealing flow increases, the swirl ratio undergoes a steep drop up to $\Phi_0 \approx 0.068$ ($PFR = 1$), where both curves flatten.

5.1.2. Effect of Vane and Strut Clocking

Figure 6a includes the pressure coefficient profiles inside the DHC for the tested HPT vane clocking arrangements at $PFR = 0$ and $PFR = 1$. The data are acquired at $\Delta\theta_S/\theta_S = 0$, i.e., with the taps aligned to the strut LE. The vane clocking effect can penetrate the DHC up to $x \approx 0.96$ without injection, while for $x < 0.96$ all the clocking cases collapse onto the same profile. At $PFR = 1$, the penetration is lower (up to $x \approx 0.98$) and the maximum C_P variation generated by the clocking is smaller. Although the impact of the individual clocking positions remains unclear, the case $\Delta\theta_V/\theta_V = 0.7$ (squared markers) features the highest pressure at $x = 1$, for both purge conditions.

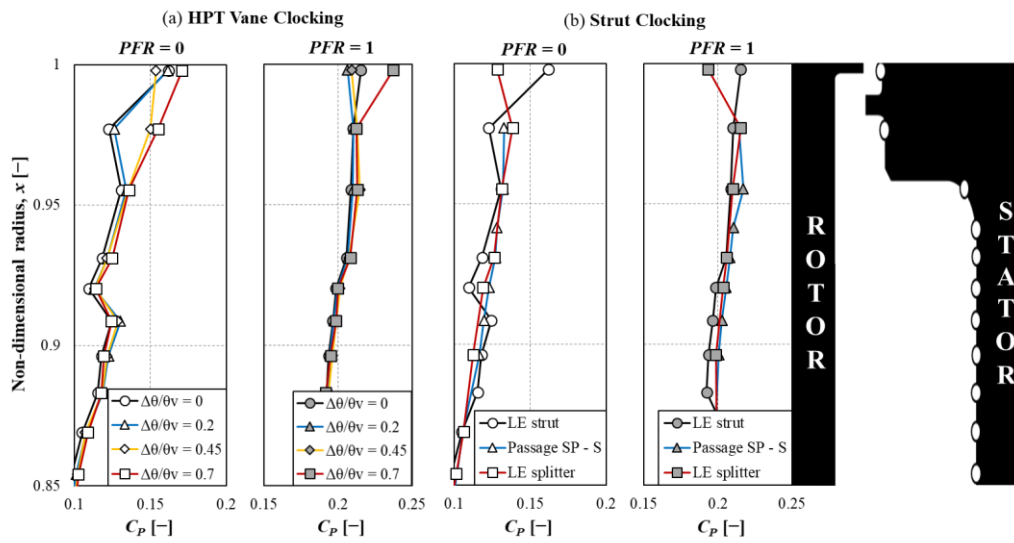


Figure 6. Radial pressure coefficient profiles inside the DHC: (a) with varying HPT vane clocking ($\Delta\theta_V/\theta_V$); (b) with varying strut clocking ($\Delta\theta_S/\theta_S$). Data at $PFR = 0$ (left) and $PFR = 1$ (right) are shown for both cases.

The strut clocking effect is evaluated in Figure 6b, at $PFR = 0$ and $PFR = 1$. In this case, the HPT vane position is kept nominal ($\Delta\theta_V/\theta_V = 0$). The penetration appears higher for the strut clocking than for the vane clocking, with perturbations detected up to $x \approx 0.91$ at $PFR = 0$. Once again, the sealing air tends to suppress the influence of clocking in the cavity, reducing the maximum C_p variation and its penetration in the cavity, as evidenced by the $PFR = 1$ radial lines. The pressure measured in front of the strut LE (squared markers) always tops the one at the splitter II-strut mid-passage (circular markers) for $x = 1$, due to the strut potential effect (the splitter LE tap is not available for this comparison). Although not shown in the paper, data at $PFR = 2$ are also acquired and analyzed, confirming the qualitative trends observed between the no-purge and the nominal conditions, both in terms of HPT vane and strut clocking.

5.1.3. Sealing Performance

The sealing effectiveness, calculated sampling DHC fluid from the stator taps at $x = 1$ (white markers) and $x = 0.93$ (black markers), is plotted in Figure 7a as a function of the sealing flow parameter for all the tested purge mass flows. As expected, the effectiveness generally increases with Φ_0 , and the values obtained outside of the rim seal are generally lower than the ones inside the cavity, taken at the same PFR . All the represented datasets, corresponding to different HPT vane clocking configurations, show a plateau for $\Phi_0 > 0.068$ ($PFR = 1$). This value can thus be associated with the minimum sealing flow rate to prevent ingress ($\Phi_0 = \Phi_{0,min} \approx 0.068$). The maximum effectiveness at $x = 1$ is $\varepsilon \approx 0.90 < 1$, demonstrating that, outside of the stator lip, the annulus flow penetrates the rotor-stator gap even with high purge mass flows. On the other hand, the maximum effectiveness at $x = 0.93$ is $\varepsilon = 0.99 \approx 1$ (within the uncertainty of the analyzer). Therefore the rim seal is capable, with a suitable purge air supply, of guaranteeing fully sealed operation in the wheel space. The fact that $\Phi_{0,min}$ is in the proximity of the nominal case means that the DHC is properly designed to suppress hot annulus flow ingestion in normal operating conditions without injecting excessive coolant, which would diminish the turbine efficiency. $\Phi_{0,min}$ obtained in this work is much higher than the value obtained by Scobie et al. [7] for a similar DHC ($\Phi_{0,min} \approx 0.033$): the difference in annulus Mach number ($M < 0.2$ for [7]) is identified as the main cause of the discrepancy, leading higher Re_W and $C_{0,min}$. As a counterproof, the minimum sealing flow rate is closer to the outcome of [10] ($\Phi_{0,min} \approx 0.09$), obtained for an upstream radial-clearance seal, but with $M \approx 0.4$.

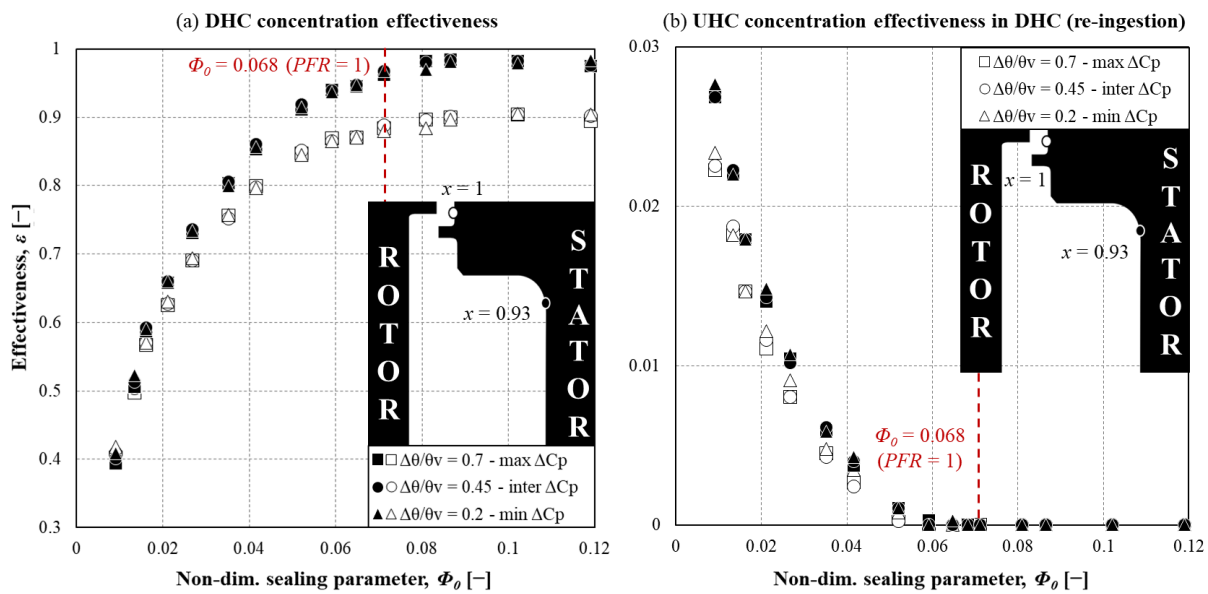


Figure 7. Concentration effectiveness as a function of the DHC sealing flow parameter: (a) in the DHC; (b) in the UHC. Data are acquired in the DHC at $x = 0.93, 1$ for both cases.

The marker shapes in Figure 7a symbolize different vane clocking positions, which practically collapse all on the same curves, one for each measurement location. As indicated in the legend of the plot, the clocking positions correspond to different $\Delta C_{P,max} = \max[C_P(\theta)] - \min[C_P(\theta)]$, where $C_P(\theta)$ are the pressure coefficients retrieved from the first array of wall taps on the TVF hub wall ($z/L_{c,z} = 0.28$). In the following section, it will be shown that at $PFR = 1$, $\Delta\theta_V/\theta_V = 0.2$ returns the minimum $\Delta C_{P,max}$, $\Delta\theta_V/\theta_V = 0.7$ the maximum $\Delta C_{P,max}$, and $\Delta\theta_V/\theta_V = 0.45$ an intermediate $\Delta C_{P,max}$. Contrary to what is expected from the traditional models/correlations (see the Introduction section), in which the predicted $\Phi_{0,min}$ is proportional to $\Delta C_{P,max}^{0.5}$, the results reveal the insensitivity of the sealing performance to the vane clocking arrangement, thus to $\Delta C_{P,max}$. Such an outcome is in line with the findings of Hualca et al. [9], who varied $\Delta C_{P,max}$ by axially displacing the upstream vane row. This suggests that the mentioned models may not provide the most appropriate description of the ingress phenomenon for the setup under examination, where the presence of upstream and downstream airfoils generates a complex hub flow field, and the annulus Reynolds and Mach are relatively high. In this sense, Graikos et al. [11] recently proposed a novel interpretation of ingress, correlated to the swirl ratio difference between annulus and rim seal clearance rather than to $\Delta C_{P,max}$. Unfortunately, the test vehicle is not equipped for annulus swirl ratio measurements at the axial location of the DHC gap, which could back up their interpretation.

The dual-channel configuration of the gas analyzer is exploited by seeding the HPT upstream hub cavity (UHC) with a different gas in order to evaluate the UHC purge re-ingestion in the DHC. The results are illustrated in Figure 7b, with varying DHC purge mass flow. For all the measured data, the UHC PFR is maintained at 1 (nominal mass flow). The UHC effectiveness is maximum with small Φ_0 in the DHC, indicating relatively high re-ingestion levels when little to no DHC sealing flow is injected. Interestingly, ϵ at $x = 0.93$ appears higher than at $x = 1$: this is ascribed to the presence of small leaks between the UHC and the DHC through the rotor blade roots at $x > 0.96$, where the silicone sealant locally deteriorated. Even for the case $\Phi_0 = 0.009$, where the leakage shows the highest impact in the effectiveness chart, its mass flow is estimated to be marginal ($< 1\%$ of the DHC injection), hence aerodynamically negligible. Finally, the HPT vane clocking does not produce relevant changes in the amount of re-ingestion, as also found for the DHC purge effectiveness.

5.1.4. Oil Flow Visualization

The pseudo-streamlines obtained with the oil flow visualization are presented in Figure 8. The rotor and stator pictures are limited to $x < 0.6$ and $0.7 < x < 1$, respectively,

hiding confidential mechanical details. Figure 8a reports a scheme of the flow structures expected in a rotor-stator cavity with sealing flow injection to be compared with the experimental results. The fact that the sealing configuration in the scheme is different from the tested rim seal is irrelevant to the current discussion. A Batchelor-like flow structure is thought to form in the cavity [30]: the fluid moves radially inwards on the stator boundary layer and outwards on the rotor one, while the inviscid core rotates at a fraction of the rotor speed and transports fluid from the stator boundary layer to the rotor one. According to the Taylor-Proudman theorem, no axial and tangential velocity gradients are present in the core, and the radial velocity is zero.

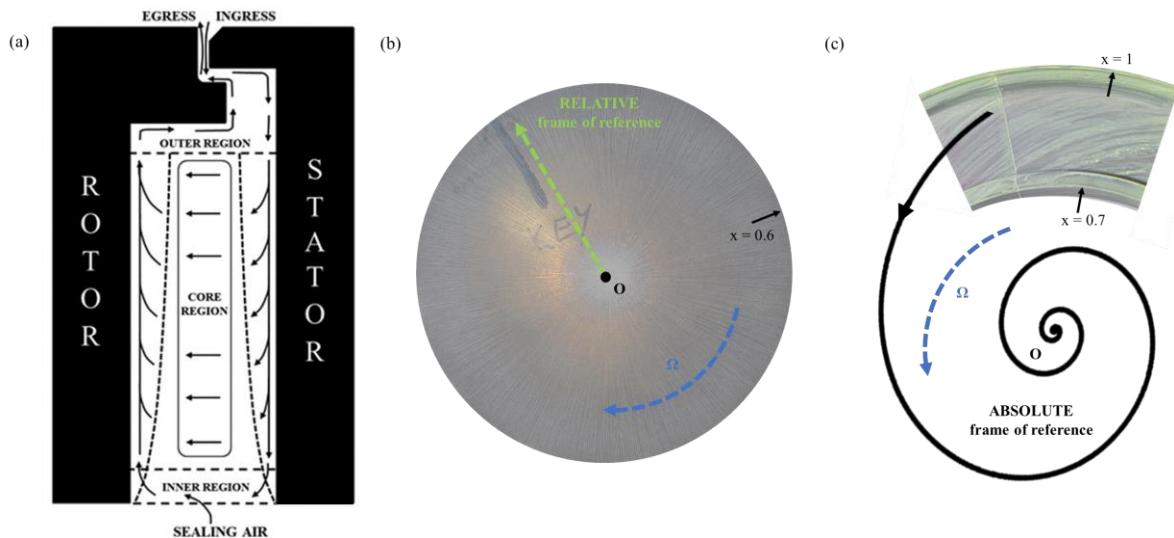


Figure 8. Flow structures in the DHC: (a) theoretical scheme, adapted from Patinios et al. [31]; (b) oil flow visualization results (rotor side); (c) oil flow visualization results (stator side). Oil flow visualization is performed at $PFR = 1$ and $\Delta\theta_V/\theta_V, \Delta\theta_S/\theta_S = 0$.

The wall shear stress trajectories on the rotor wall (Figure 8b) appear as straight lines (green arrow) departing from the center of the rotor and spreading radially outwards due to the disk pumping effect on the boundary layer flow. As explained in Section 3.2.4, the rotor disk was not initially painted with oil, meaning that the pattern is produced by the stator boundary layer air, feeding the rotor boundary layer. Being on the rotor disk, the straight lines represent the flow motion in the relative frame of reference: after including the contribution of the rotor speed (blue arrow), the stress trajectories in the absolute frame of reference would appear as spirals. The pigment pattern on the stator wall (Figure 8c) also assumes the shape of spirals, produced by the combination of the flow absolute tangential velocity in the same direction of the rotor speed, and the absolute radial velocity, directed inwards to satisfy the continuity in the DHC. The pseudo-streamlines are in agreement with the theoretical model, and, to the authors' knowledge, they constitute the first open-literature example of oil flow visualization inside an engine-representative cavity.

5.2. Time-Averaged Flow on the Stator Platform

5.2.1. Pressure Measurements—Effect of the Sealing Flow Rate

The circumferential pressure coefficient profiles, acquired at $z/L_{c,z} = 0.28$, are displayed in Figure 9a, for $PFR = 0, 0.5, 1, 1.5, 2$. Although the stage total pressure ratio is kept constant during the tests, the secondary air injection causes local boundary layer energization on the TVF hub platform, resulting in a static pressure decrease when the PFR rises. The analytical model, described by Equation (11), has been fitted to all the investigated cases but is here reported only for the extremes $PFR = 0$ (dotted line) and $PFR = 2$ (dashed line). The agreement with experimental data is very good, and the adjusted coefficient of determination, averaged across the tested PFR s, is $R_{adj}^2 \approx 0.9$. The

model is capable of capturing the low-spatial-frequency oscillations related to the TVF struts, as well as the high-spatial-frequency peaks derived from the HPT vanes. By plotting the amplitude ratio k_V/k_S against Φ_0 , as in Figure 9b, the relative contribution of the vane and the strut pressure fields on the hub circumferential distribution is assessed. The amplitude of the vane-related pressure oscillations (propagating downstream) is consistently about 30% of the strut-related oscillations (propagating upstream) for $\Phi_0 < 0.054$ ($PFR = 0.8$). The k_V/k_S ratio then experiences a sudden drop, with the minimum found at $\Phi_0 = 0.068 \approx \Phi_{0,min}$ ($PFR = 1$), where the vane-related amplitude is only 20% of the strut-related amplitude. Finally, the amplitude ratio undergoes a steep increase for $\Phi_0 > \Phi_{0,min}$, reaching approximately 45% at $\Phi_0 = 0.135$ ($PFR = 2$).

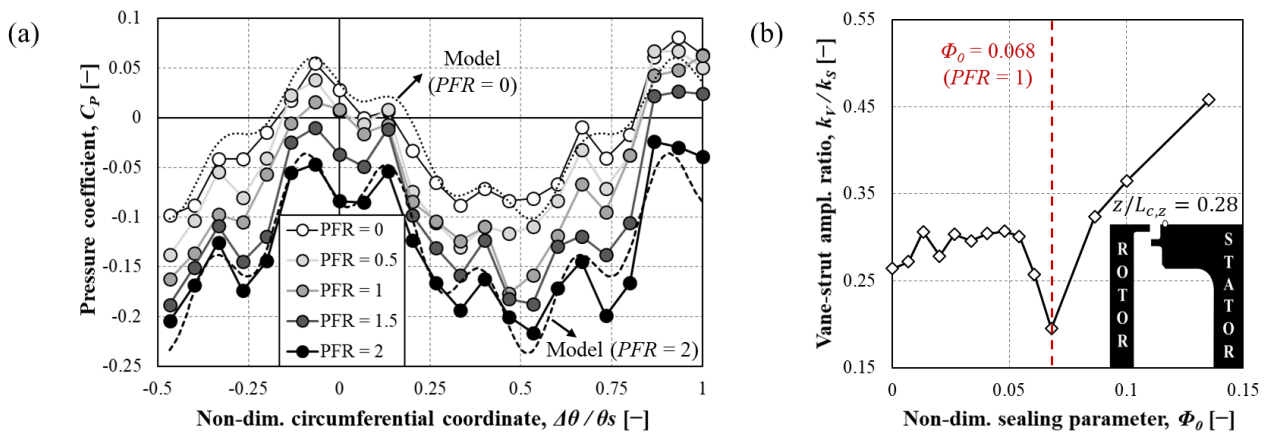


Figure 9. Pressure coefficient on the TVF hub platform: (a) circumferential profiles with varying PFR; (b) vane-strut amplitude ratio, estimated from the analytical model in Equation (11), as a function of the sealing flow parameter. Experimental and model results are for $z/L_{c,z} = 0.28$ and $\Delta\theta_V/\theta_V = 0$.

A non-monotonic behavior is also observed for the variation of $\Delta C_{P,max}$ over Φ_0 , depicted by the white diamonds in Figure 10a. The peak-to-through pressure coefficient variation reaches a maximum at $\Phi_0 = 0.068 \approx \Phi_{0,min}$ ($PFR = 1$). In other words, the minimum sealing flow rate to prevent ingress is the one that faces the largest $\Delta C_{P,max}$. This indicates a tight connection between $\Phi_{0,min}$ and $\Delta C_{P,max}$ exists, although Figure 7 seems to refute $\Delta C_{P,max}$ as the main driver for ingress. The average C_p (black diamonds) has instead a monotonic decreasing trend, already evidenced in Figure 9a and associated to the stator platform boundary layer energization. More specifically, for low purge injection rates, the interaction between ingress and egress flows is thought to form a recirculation zone [32] in the outer region, leading to increased blockage ahead of the stator hub surface and thus, higher static pressure. At high PFRs, the recirculation disappears, the purge flow travels radially up to the rotor seal lip and then is deflected onto the stator platform, lifting up the annulus fluid and locally increasing the velocity in the boundary layer, with a corresponding pressure drop.

The trend of $\Delta C_{P,max}$ and average C_p , moving axially downstream of the cavity on the stator platform, is represented in Figure 10b, for five PFRs. The peak-to-through difference (squared marker) is maximum in the proximity of the cavity, reaches a minimum between $z/L_{c,z} = 0.71$ and $z/L_{c,z} = 2.12$, then increases again at higher $z/L_{c,z}$. This development is related to the vane-strut contribution on the hub circumferential pressure profile: the decay of the vane-related amplitudes is predominant immediately downstream of the DHC, causing the local minimum; approaching the strut LEs, the strut-related oscillations intensify and overcompensate the previously described effect, leading to higher $\Delta C_{P,max}$. The PFR influence loses strength moving further from the stator-rotor gap, becoming negligible at $z/L_{c,z} = 6.36$. The average C_p (diamond markers) rapidly rises on the TVF hub platform, consistently with the annulus geometry: in fact, the first bent of the S-shaped duct is known to produce a hub (+)-to-shroud (-) pressure gradient [33]. Interestingly, the average pressure decrease with purge, observed in Figure 10a, is completely reversed in

the interval $z/L_{c,z} = 0.71 - 2.12$, after which C_p grows with higher PFR s. The behavior is attributed to the purge injection impact on the average tangential velocity in the near-end wall region, which affects the radial equilibrium in the annulus.

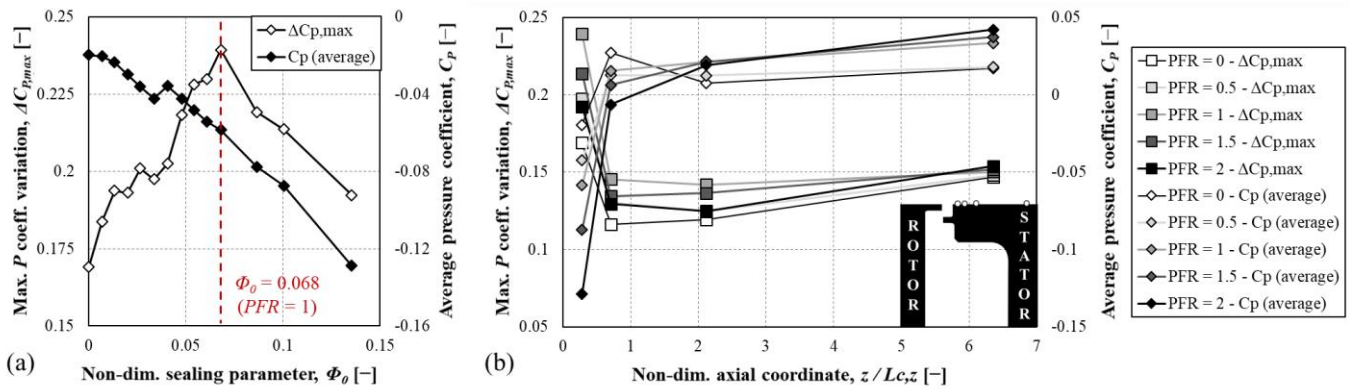


Figure 10. Annulus pressure coefficient, peak-to-trough variation and average value: (a) at $z/L_{c,z} = 0.28$, as a function of the sealing flow parameter; (b) as a function of the axial distance from the cavity, for a selection of PFR s. Data are acquired at $\Delta\theta_V/\theta_V = 0$.

5.2.2. Pressure and Effectiveness Measurements—Effect of Vane Clocking

Figure 11 includes a side-by-side comparison of the pressure coefficient, measured on the TVF hub platform at $z/L_{c,z} = 0.28$, and the corresponding DHC concentration effectiveness, calculated from the same wall taps. The plots allow us to evaluate both the effect of the sealing flow rate ($PFR = 0, 1, 2$) and the effect of the HPT vane clocking ($\Delta\theta_V/\theta_V = 0, 0.2, 0.7$). Since it is not possible to perform concentration measurements without seed gas, thus without purge, the $PFR = 0.2$ is plotted in Figure 11d instead of $PFR = 0$. As anticipated in Section 5.1.3, Figure 11b indicates that at $PFR = 1$, $\Delta C_{p,max}$ for $\Delta\theta_V/\theta_V = 0.7$ is about 10% larger than the same value for $\Delta\theta_V/\theta_V = 0$ and 25% larger than the value for $\Delta\theta_V/\theta_V = 0.2$ (the $\Delta\theta_V/\theta_V = 0.45$ case, not reported here, is analogous to the $\Delta\theta_V/\theta_V = 0$ case in terms of $\Delta C_{p,max}$). The point-to-point pressure difference is high at some locations (e.g., around $\Delta\theta/\theta_S = 0.5$ in Figure 11a). In fact, the measurement resolution is limited by the size of the stator platform and of the taps' lead-out paths, which have to fit inside the hollow struts. Nonetheless, the curves are in good agreement with the analytical model in Equation (11), with proper values of the fitting parameters. The purge increase is responsible for the reduction of average C_p in Figure 11a–c (from left to right), already described in Section 5.2.1. At the same time, the average ε level increases (Figure 11d–f, from left to right). Interestingly, the case of overall maximum $\Delta C_{p,max}$, which is $PFR = 1$ and $\Delta\theta_V/\theta_V = 0.7$ (red line in Figure 11b), coincide with the one of maximum $\Delta\varepsilon_{max}$ (red line in Figure 11e), where $\Delta\varepsilon_{max} = \max[\varepsilon(\theta)] - \min[\varepsilon(\theta)]$. Moreover, the k_V/k_S ratio was found to be maximum for $PFR = 2$ (see Section 5.2.1): this explains why, in the profiles of Figure 11c, the vane-related periodicity is more pronounced than the strut-related one. The k_V/k_S trend also influences the effectiveness curves in Figure 11f, where the θ_S -periodic oscillation is barely recognizable.

When looking at the tangential C_p and ε asymmetries, the observed overall trend is that low pressure corresponds to high effectiveness and vice versa. Such a trend can be better appreciated in Figure 12, where the C_p (squared markers) and ε (circular markers) data for $PFR = 1$ and $\Delta\theta_V/\theta_V = 0$ are singled out. The two profiles are almost in opposition to phase, with only a slight circumferential shift. All the considerations above point to the conclusion that, although the pressure hub profile appears not to affect $\Phi_{0,min}$, it remains the main driver for the distribution of the cavity egress inside the annulus. The same conclusion is reached by Scobie et al. [7], although, in their experiments, the high-effectiveness peaks are aligned with the high-pressure peaks.

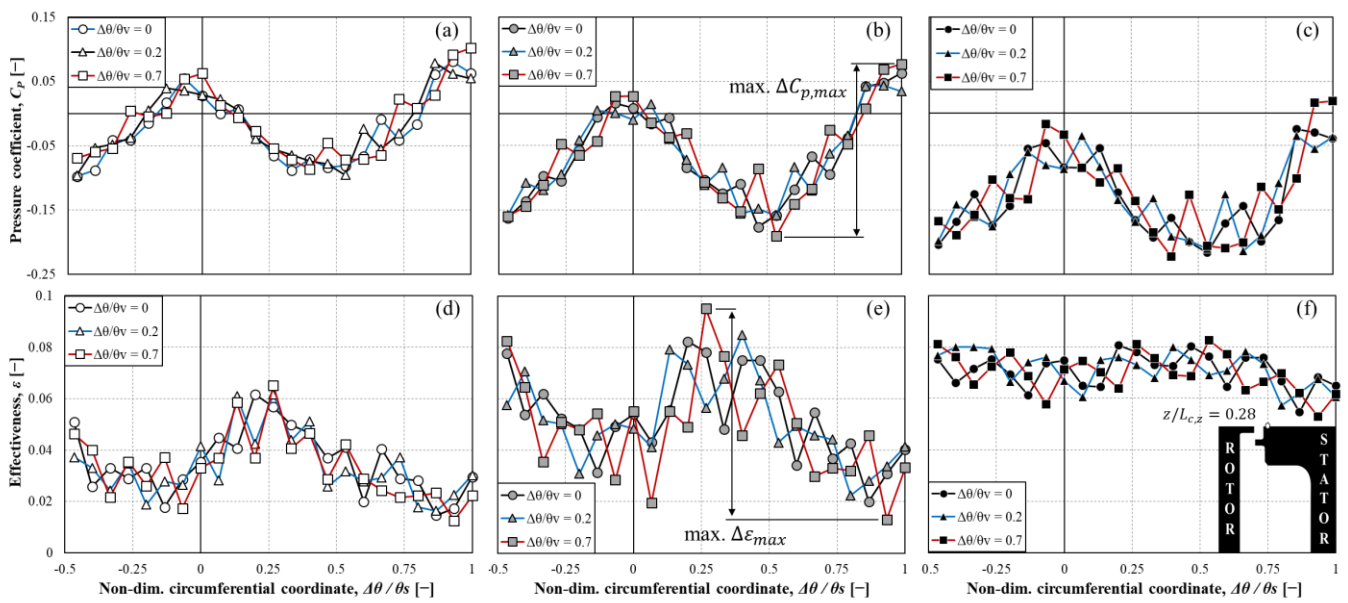


Figure 11. Annulus pressure coefficient circumferential profiles for: $PFR = 0$ (a), $PFR = 1$ (b), and $PFR = 2$ (c). Annulus effectiveness circumferential profiles for $PFR = 0.2$ (d), $PFR = 1$ (e), and $PFR = 2$ (f). Data are acquired at $z/L_{c,z} = 0.28$ and $\Delta\theta_V/\theta_V = 0, 0.2, 0.7$.

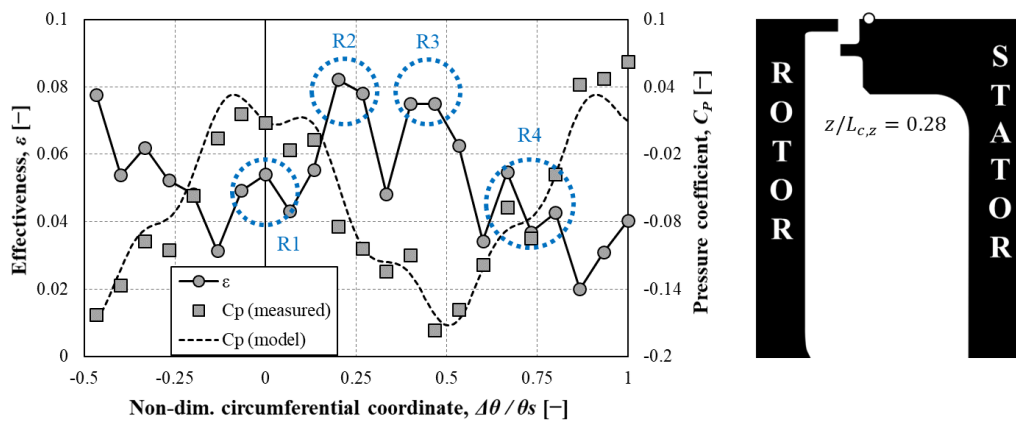


Figure 12. Annulus pressure coefficient and circumferential effectiveness profiles for $PFR = 1$. Data are acquired at $z/L_{c,z} = 0.28$ and $\Delta\theta_V/\theta_V = 0$. Both measured (grey squares) and modeled (dashed line) pressure coefficients are plotted. High-effectiveness peaks are indicated by the labels R1–R4.

5.2.3. Oil Flow Visualization

A picture of the oil flow traces on the TVF hub wall is reported in Figure 13. Since the oil-pigment mixture is injected through the DHC stator wall taps (see the Experimental Setup section), the colored pattern represents the sealing flow distribution on the downstream hub surface across a full TVF strut pitch ($\Delta\theta_S/\theta_S = 0 - 1$, as indicated by the red text and dashed lines). Such distribution can be therefore compared to the concentration effectiveness circumferential profile in Figure 12. The figures show good agreement in terms of correspondence between pigment streaks and effectiveness peaks. More specifically, four regions with heavy residues of pigment, interspersed by as many uncolored areas, are highlighted in Figure 13 by the blue dotted circles and labeled as R1 – R4. The circumferential position of R1 – R4 matches the position of the local ϵ maxima in Figure 12, suggesting that the adopted visualization technique is suitable to qualitatively study the egress phenomenon.

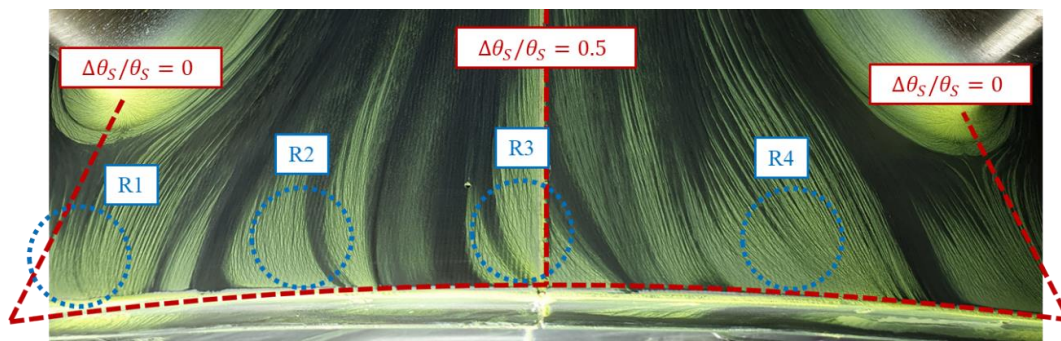


Figure 13. Oil flow visualization in the annulus (stator hub platform) for $PFR = 1$ and $\Delta\theta_V/\theta_V = 0$. Regions with high pigment accumulation are indicated by the labels R1–R4.

5.3. Time-Resolved Pressure Measurements Inside the DHC

The unsteady pressure fluctuations, measured at $PFR = 1$ and $\Delta\theta_S/\theta_S = 0$, are depicted in Figure 14 for three radial positions ($x = 0.92, 0.98, 1$). All the spectra are dominated by the HPT blade passing frequency component ($f = 1 \cdot BPF$), which reaches up to 2 – 2.6% of the reference pressure, depending on the radial sensor location. Additionally, secondary peaks are visible at the BPF harmonics ($f = 2 \cdot BPF, 3 \cdot BPF, 4 \cdot BPF$). While the investigated radial positions show comparable amplitudes at the BPF , the outermost sensor ($x = 1$, outside of the stator seal lip) always measures the highest magnitude at the BPF multiples. A minor peak is spotted at $f \approx 0.63 \cdot BPF$, which corresponds to a linear combination of the HPT and LPT blade passing frequencies: Merli et al. [34] also found pressure fluctuations with the mentioned periodicity in the annulus, upstream of the TVF struts. No non-synchronous components, which could be associated with rotating flow modes [18], are detected with the current measurement setup, at least not in the same order of magnitude as the BPF -related components.

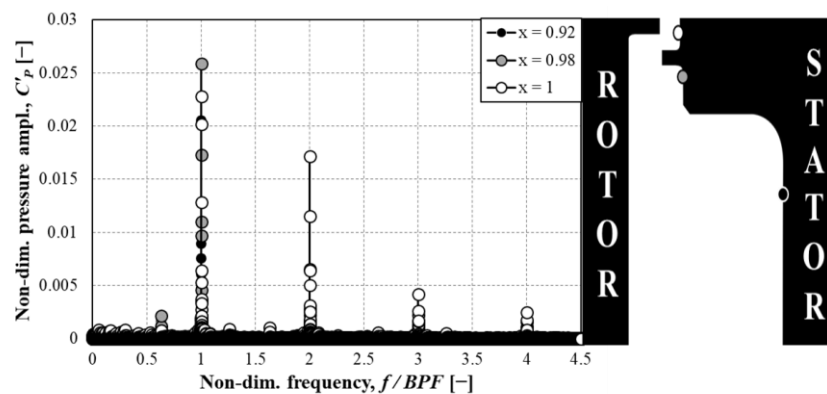


Figure 14. Non-dimensional pressure spectra at different radial positions in the DHC. Data are acquired at $PFR = 1$, $x = 0.92, 0.98, 1$ and $\Delta\theta_V/\theta_V, \Delta\theta_S/\theta_S = 0$.

The effects of sealing flow rate and strut clocking on the non-dimensional BPF pressure component ($C'_{P,BPF}$) are evaluated in Figure 15. In particular, the figure compares $C'_{P,BPF}$ at $\Delta\theta_S/\theta_S = 0$ (strut LE, black line) and $\Delta\theta_S/\theta_S = 1/3$ (splitter LE, red line) across the investigated Φ_0 range. Figure 15a shows the results for $x = 0.92$: two local maxima are found, at approximately $\Phi_0 = 0.02$ and $\Phi_0 = 0.068$. The strut clocking effect seems not to penetrate the analyzed location inside the DHC, as the two curves are almost overlapping. Figure 15b illustrates the results for $x = 1$: the fluctuations at $f = BPF$ are generally higher compared to the previous case and, in terms of strut clocking, the fluctuations at $\Delta\theta_S/\theta_S = 1/3$ (red line) are more intense. The trend with PFR is diametrically opposite to what is reported in Figure 15a: low $C'_{P,BPF}$ values are measured for $\Phi_0 \leq 0.02$, then the oscillations rise up to a maximum before $\Phi_0 = 0.068$, where a sudden drop is noticed.

Interestingly, such behavior is analogous to the k_V/k_S curve in Figure 9b, suggesting that the periodic unsteadiness is driven by the interaction of the vane-strut steady pressure field with the time-dependent blade contribution.

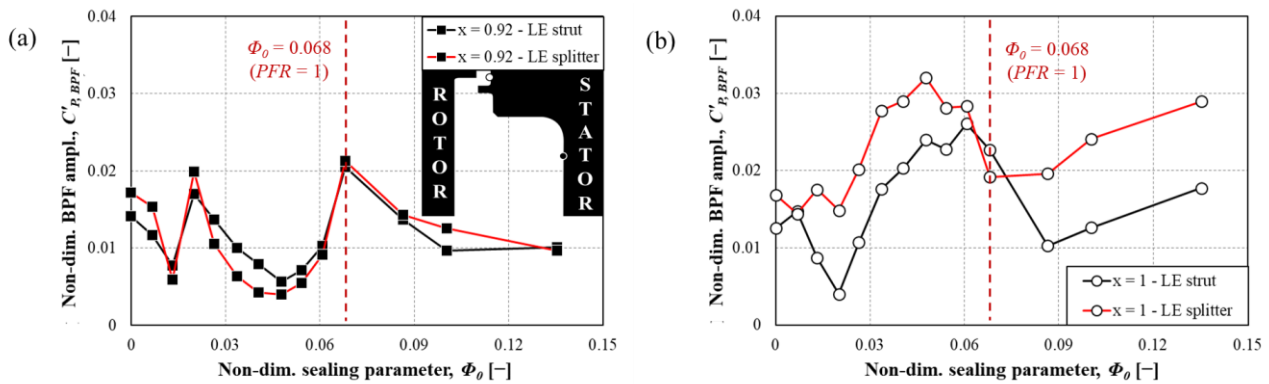


Figure 15. Non-dimensional pressure amplitude at $f = 1 \cdot BPF$ as a function of the sealing flow parameter for two strut clocking positions ($\Delta\theta_S/\theta_S = 0, 2/3$). (a) Results at $x = 0.92$. (b) Results at $x = 1$. Data are acquired at $\Delta\theta_V/\theta_V = 0$ for both cases.

Finally, the C'_p spectra with different HPT vane clocking arrangements ($\Delta\theta_V/\theta_V = 0.2, 0.45, 0.7$) are plotted in Figure 16. As expected from the analysis of the pneumatic measurements, no significant change is noticeable at $x = 0.92$ (Figure 16a), where the vane clocking effect appears not to penetrate. Conversely, at $x = 1$ (Figure 16b), the configuration $\Delta\theta_V/\theta_V = 0.45$, indicated with the diamond markers and corresponding to an intermediate $\Delta C_{p,max}$, shows a $1 \cdot BPF$ component about 75% larger than both the other cases.

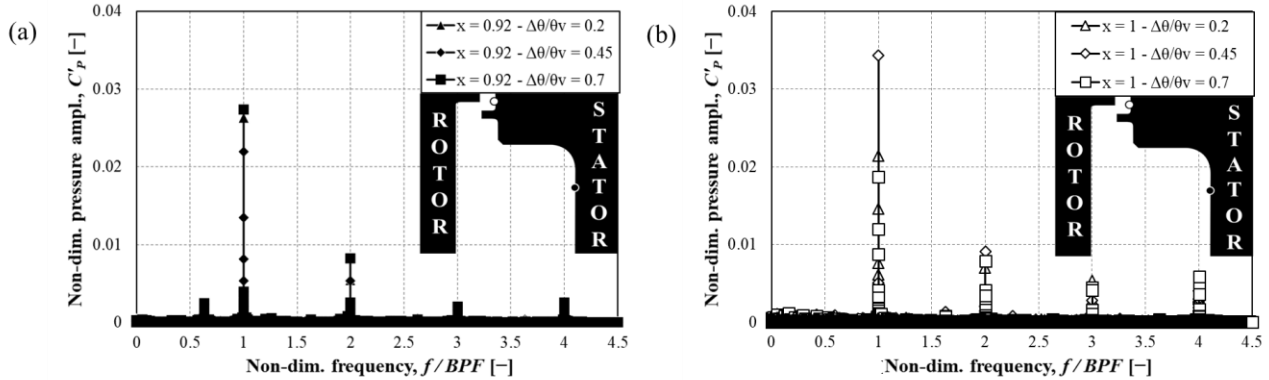


Figure 16. Non-dimensional pressure spectra at different HPT vane clocking positions ($\Delta\theta_V/\theta_V = 0.2, 0.45, 0.7$). (a) Results at $x = 0.92$. (b) Results at $x = 1$. Data are acquired at $PFR = 1$ and $\Delta\theta_S/\theta_S = 0$.

6. Conclusions

The paper presents the outcome of steady and unsteady measurements inside the downstream hub cavity of an HPT stage integrated into a two-stage turbine setup. The engine-relevant test vehicle and the realistic annulus flow conditions adopted in the study constitute an important novelty with respect to the available literature on the topic. The steady measurements consist of both aerodynamic (pressure) measurements inside the wheel space and on the stator platform and concentration effectiveness measurements. Additionally, unsteady pressure measurements and oil flow visualization are carried out to further characterize the cavity flow features. A large number of sealing flow rates is investigated, extending from $PFR = 0$ to $PFR = 2$. The effects of the HPT vane and TVF strut clocking are also assessed.

The static pressure on the DHC stator wall linearly increases with PFR , thus with Φ_0 . The swirl ratio in the cavity is maximum at $PFR = 0$ and steeply decreases with the sealing flow rate up to $\Phi_0 \approx 0.068$ ($PFR = 1$), where its sensitivity to the injection drops.

For the case without purge, the pressure variation due to vane and strut clocking is found to penetrate up to $x = 0.95$ and $x = 0.9$ inside the DHC, respectively. The purge injection reduces both the radial penetration and the strength of the pressure variation.

The concentration effectiveness data reveal that for $\Phi_0 \geq 0.068 = \Phi_{0,min}$ ($PFR \geq 1$), ingress is mainly confined to the rim seal region ($x > 0.93$), which, in real engine applications, can be protected with heat-resistant alloys. Moreover, re-ingestion of the upstream hub cavity sealing flow is detected for low DHC injection rates.

The pressure on the TVF hub platform is fitted to an analytical model, which allows isolating the vane and strut contributions on the measured circumferential profile. The average pressure in the annulus decreases with higher PFR s, while the peak-to-trough variation is maximized at $\Phi_{0,min}$. Additionally, $\Delta C_{P,max}$ varies with the HPT vane clocking, but this is demonstrated to have negligible impact on the value of $\Phi_{0,min}$. This appears in contrast with the traditional ingress models, developed in less engine-representative test environments. Further analyses would be required to consolidate the limits of the mentioned models in testbeds of similar complexity. Nevertheless, the hub pressure profile predominantly drives the distribution of the DHC egress inside the annulus, as confirmed by the effectiveness of circumferential profiles and the oil flow visualization.

Finally, the unsteady pressure spectra are dominated by the BPF component and its harmonics for each tested purge and clocking condition. No non-synchronous oscillations with the same order of magnitude are identified. Higher harmonics of the BPF are particularly strong at $x = 1$, and they are partially suppressed inside the cavity. At the same time, the $1 \cdot BPF$ component shows minor strut and vane clocking effects at $x = 0.92$, coherently with the pneumatic measurements. Such effects are instead considerable at $x = 1$, where the sensor at $\Delta\theta_S/\theta_S = 2/3$ and the vane clocking position $\Delta\theta_V/\theta_V = 0.45$ have the highest BPF -periodic fluctuations.

Author Contributions: Conceptualization, M.P. and E.G.; methodology, F.M. and M.P.; software, F.M. and M.P.; validation, F.M., N.K. and A.H.; formal analysis, F.M. and M.P.; investigation, F.M., N.K., A.H. and M.P.; resources, N.K. and A.H.; data curation, F.M.; writing—original draft preparation, F.M.; writing—review and editing, M.P. and E.G.; visualization, F.M.; supervision, E.G.; project administration, E.G.; funding acquisition, E.G. All authors have read and agreed to the published version of the manuscript.

Funding: The project leading to this application has received funding from the Clean Sky 2 Joint Undertaking under the European Union's Horizon 2020 research and innovation program (grant agreement No 785313).

Institutional Review Board Statement: Not applicable.

Informed Consent Statement: Not applicable.

Data Availability Statement: Restrictions apply to the availability of the data presented in this study. The data are available on request from the corresponding author, prior authorization of GE Aviation.

Acknowledgments: The authors would like to thank F. Mangini for his contribution in operating the test facility and GE Aviation for the permission to publish this paper.

Conflicts of Interest: The authors declare no conflict of interest. The funders had no role in the design of the study; in the collection, analyses, or interpretation of data; in the writing of the manuscript; or in the decision to publish the results.

Nomenclature

Abbreviations

BPF	blade passing frequency
DFT	discrete Fourier transform
HPT, LPT	high-pressure, low-pressure turbine
ITD	intermediate turbine duct
LE	leading edge

PFR	purge flow ratio
TVF	turbine vane frame
UHC, USC	upstream hub/shroud cavity
DHC, DSC	downstream hub/shroud cavity
Symbols	
z, r, θ	axial, radial, tangential coordinate
V, S, SP	HPT vane, TVF strut, TVF splitter
b	rotor lip inner radius
c	concentration
C	non-dimensional coefficient
f, t	frequency, time
G	gap ratio
k, φ	pressure model amplitude, phase
L	length
\dot{m}	mass flow
P	pressure
Re	Reynolds number
V	core absolute velocity
W, M	annulus absolute velocity
x	non-dimensional radius
β	swirl ratio
ε	concentration effectiveness
λ_T	turbulent flow parameter
ρ, μ	density, dynamic viscosity
Φ	non-dimensional sealing parameter
Ω	disk rotational speed
Subscripts and Superscripts	
$0, a, s$	cavity, annulus, sample
c	clearance
des	design vane position
F	flow
in	inner seal
min	minimum sealing flow
max	peak-to-trough difference
P	pressure
T	total
W	annulus
Ω	rotational
$-$	average component
$'$	time-dependent component

References

- Owen, J.M. Prediction of Ingestion Through Turbine Rim Seals—Part II: Externally Induced and Combined Ingress. *J. Turbomach.* **2010**, *133*, 11. [[CrossRef](#)]
- Regina, K.; Kalfas, A.I.; Abhari, R.S. Experimental Investigation of Purge Flow Effects on a High Pressure Turbine Stage. *J. Turbomach.* **2014**, *137*, 41006. [[CrossRef](#)]
- Phadke, U.P.; Owen, J.M. Aerodynamic aspects of the sealing of gas-turbine rotor-stator systems: Part 3: The effect of nonaxisymmetric external flow on seal performance. *Int. J. Heat Fluid Flow* **1988**, *9*, 113–117. [[CrossRef](#)]
- Bohn, D.; Wolff, M. Improved Formulation to Determine Minimum Sealing Flow— $C_{w, min}$ —for Different Sealing Configurations. In Proceedings of the ASME Turbo Expo 2003, Collocated with the 2003 International Joint Power Generation Conference, Atlanta, GA, USA, 16–19 June 2003; Volume 5.
- Hamabe, K.; Ishida, K. Rim Seal Experiments and Analysis of a Rotor-Stator System With Nonaxisymmetric Main Flow. In Proceedings of the ASME 1992 International Gas Turbine and Aeroengine Congress and Exposition, Cologne, Germany, 1–4 June 1992; Volume 1: Turbomachinery.

6. Chew, J.W.; Green, T.; Turner, A.B. Rim Sealing of Rotor-Stator Wheelspaces in the Presence of External Flow. In Proceedings of the ASME 1994 International Gas Turbine and Aeroengine Congress and Exposition, The Hague, The Netherlands, 13–16 June 1994; Volume 1: Turbomachinery.
7. Scobie, J.A.; Hualca, F.P.; Sangan, C.M.; Lock, G.D. Egress Interaction Through Turbine Rim Seals. *J. Eng. Gas Turbines Power* **2018**, *140*, 4. [[CrossRef](#)]
8. Scobie, J.A.; Hualca, F.P.; Patinios, M.; Sangan, C.M.; Owen, J.M.; Lock, G.D. Re-Ingestion of Upstream Egress in a 1.5-Stage Gas Turbine Rig. *J. Eng. Gas Turbines Power* **2018**, *140*, 4. [[CrossRef](#)]
9. Hualca, F.P.; Horwood, J.T.M.; Sangan, C.M.; Lock, G.D.; Scobie, J.A. The Effect of Vanes and Blades on Ingress in Gas Turbines. *J. Eng. Gas Turbines Power* **2020**, *142*, 1. [[CrossRef](#)]
10. Sangan, C.M.; Pountney, O.J.; Zhou, K.; Wilson, M.; Owen, J.M.; Lock, G.D. Experimental Measurements of Ingestion Through Turbine Rim Seals—Part I: Externally Induced Ingress. *J. Turbomach.* **2012**, *135*, 11.
11. Graikos, D.; Tang, H.; Sangan, C.M.; Lock, G.D.; Scobie, J.A. A New Interpretation of Hot Gas Ingress Through Turbine Rim Seals Influenced by Mainstream Annulus Swirl. *J. Eng. Gas Turbines Power* **2022**, *144*, 9. [[CrossRef](#)]
12. Cao, C.; Chew, J.W.; Millington, P.R.; Hogg, S.I. Interaction of Rim Seal and Annulus Flows in an Axial Flow Turbine. *J. Eng. Gas Turbines Power* **2004**, *126*, 786–793. [[CrossRef](#)]
13. Jakoby, R.; Zierer, T.; Lindblad, K.; Larsson, J.; Bohn, L.D.E.; Funcke, J.; Decker, A. Numerical Simulation of the Unsteady Flow Field in an Axial Gas Turbine Rim Seal Configuration. In Proceedings of the ASME Turbo Expo 2004: Power for Land, Sea, and Air, Vienna, Austria, 14–17 June 2004; Volume 4: Turbo Expo 2004.
14. Roy, R.P.; Feng, J.; Narzary, D.; Paolillo, R.E. Experiment on Gas Ingestion Through Axial-Flow Turbine Rim Seals. *J. Eng. Gas Turbines Power* **2005**, *127*, 573–582. [[CrossRef](#)]
15. Beard, P.F.; Gao, F.; Chana, K.S.; Chew, J. Unsteady Flow Phenomena in Turbine Rim Seals. *J. Eng. Gas Turbines Power* **2016**, *139*, 9.
16. Savov, S.S.; Atkins, N.R.; Uchida, S. A Comparison of Single and Double Lip Rim Seal Geometries. *J. Eng. Gas Turbines Power* **2017**, *139*, 7. [[CrossRef](#)]
17. Gao, F.; Chew, J.W.; Marxen, O. Inertial waves in turbine rim seal flows. *Phys. Rev. Fluids* **2020**, *5*, 2. [[CrossRef](#)]
18. Chew, J.W.; Gao, F.; Palermo, D.M. Flow mechanisms in axial turbine rim sealing. *Proc. Inst. Mech. Eng. Part C J. Mech. Eng. Sci.* **2018**, *233*, 7637–7657. [[CrossRef](#)]
19. Marn, A.; Göttlich, E.; Cadrecha, D.; Pirker, H.P. Shorten the Intermediate Turbine Duct Length by Applying an Integrated Concept. *J. Turbomach.* **2009**, *131*, 7. [[CrossRef](#)]
20. Zerobin, S.; Aldrian, C.; Peters, A.; Heitmeir, F.; Göttlich, E. Impact of Individual High-Pressure Turbine Rotor Purge Flows on Turbine Center Frame Aerodynamics. In Proceedings of the ASME Turbo Expo 2017: Turbomachinery Technical Conference and Exposition, Charlotte, NC, USA, 26–30 June 2017.
21. Sterzinger, P.Z.; Merli, F.; Peters, A.; Behre, S.; Heitmeir, F.; Göttlich, E. Impact of Turbine–Strut Clocking on the Performance of a Turbine Center Frame. *J. Turbomach.* **2021**, *143*, 51011. [[CrossRef](#)]
22. Hubinka, J.; Santner, C.; Paradiso, B.; Malzacher, F.; Göttlich, E.; Heitmeir, F. Design and construction of a two shaft test turbine for investigation of mid turbine frame flows. In Proceedings of the ISABE, Montreal, QC, Canada, 7–11 September 2009; pp. 7–11.
23. Steiner, M.; Zerobin, S.; Bauinger, S.; Heitmeir, F.; Göttlich, E. Development and Commissioning of a Purge Flow System in a Two Spool Test Facility. In Proceedings of the 2th European Conference on Turbomachinery Fluid dynamics & Thermodynamics, Stockholm, Sweden, 3–7 April 2017.
24. Patinios, M.; Merli, F.; Hafizovic, A.; Göttlich, E. The Interaction of Purge Flows With Secondary Flow Features in Turbine Center Frames. In Proceedings of the ASME Turbo Expo 2021: Turbomachinery Technical Conference and Exposition, Virtual, 7–11 June 2021; Volume 2C: Turbomachinery—Design Methods and CFD Modeling for Turbomachinery; Ducts, Noise, and Component Interactions.
25. Bayley, F.J.; Owen, J.M. The Fluid Dynamics of a Shrouded Disk System with a Radial Outflow of Coolant. *J. Eng. Power* **1970**, *92*, 335–341. [[CrossRef](#)]
26. Daily, J.W.; Nece, R.E. Chamber Dimension Effects on Induced Flow and Frictional Resistance of Enclosed Rotating Disks. *J. Basic Eng.* **1960**, *82*, 217–230. [[CrossRef](#)]
27. Childs, P. *Rotating Flow*; Elsevier Science: Amsterdam, The Netherlands, 2010.
28. Merli, F.; Hafizovic, A.; Krajnc, N.; Schien, M.; Peters, A.; Heitmeir, F.; Göttlich, E. The Interaction of Main Stream Flow and Cavity Flows in Turbine Center Frames and Turbine Vane Frames. *J. Eng. Gas Turbines Power* **2022**, *145*, 12.
29. *MATLAB*, version 9.7.0 (R2019b); The MathWorks Inc.: Natick, MA, USA, 2019.
30. Sangan, C.M.; Lalwani, Y.; Owen, J.M.; Lock, G.D. Experimental Measurements of Ingestion Through Turbine Rim Seals: Part 5—Fluid Dynamics of Wheel-Space. In Proceedings of the ASME Turbo Expo 2013: Turbine Technical Conference and Exposition, San Antonio, TX, USA, 3–7 June 2013; Volume 3A: Heat Transfer.
31. Patinios, M.; Scobie, J.A.; Sangan, C.M.; Owen, J.M.; Lock, G.D. Measurements and Modeling of Ingress in a New 1.5-Stage Turbine Research Facility. *J. Eng. Gas Turbines Power* **2016**, *139*, 8. [[CrossRef](#)]
32. Savov, S.S.; Atkins, N.R. A Rim Seal Ingress Model Based on Turbulent Transport. In Proceedings of the ASME Turbo Expo 2017: Turbomachinery Technical Conference and Exposition, Charlotte, NC, USA, 26–30 June 2017; Volume 5B: Heat Transfer.

33. Göttlich, E. Research on the aerodynamics of intermediate turbine diffusers. *Prog. Aerosp. Sci.* **2011**, *47*, 249–279. [[CrossRef](#)]
34. Merli, F.; Krajnc, N.; Hafizovic, A.; Patinios, M.; Göttlich, E. Unsteady Investigation of Intermediate Turbine Ducts under the Influence of Purge Flows. In Proceedings of the ASME Turbo Expo 2023, Boston, MA, USA, 26–30 June 2023.

Disclaimer/Publisher’s Note: The statements, opinions and data contained in all publications are solely those of the individual author(s) and contributor(s) and not of MDPI and/or the editor(s). MDPI and/or the editor(s) disclaim responsibility for any injury to people or property resulting from any ideas, methods, instructions or products referred to in the content.